



Optimization of Heat Treatment and Cu Ions Additions to Enhance Optical and Photoluminescence Properties of Transparent Mica Glass Ceramic

S. A. M. Abdel-Hameed¹ · M. A. Ouis¹

Received: 1 December 2021 / Accepted: 11 March 2022 / Published online: 12 April 2022
© The Minerals, Metals & Materials Society 2022, corrected publication 2022

Abstract

A set of mica glasses containing copper ions were synthesized using melt quenching technique with the chemical composition $\text{Na}_{(1-X)}\text{Cu}_X\text{Mg}_3\text{AlSi}_3\text{O}_{10}\text{F}_2$, where $X=0, 0.05, 0.07, \text{ and } 0.1$. The samples were crystallized at temperatures obtained by differential thermal analysis (DTA) data. X-ray analysis confirmed the crystallization of mica ($\text{NaAl}_3\text{Si}_3\text{O}_{11}$), MgF_2 and pyrope ($\text{Mg}_3\text{Al}_2\text{Si}_3\text{O}_{12}$). Transparent glass ceramic with nano-sized crystal $< 15 \text{ nm}$ was obtained after heat treatment at $550^\circ\text{C}/4 \text{ h}+650^\circ\text{C}/0.5 \text{ h}$. The characteristic peaks of Fourier transform infrared spectroscopy (FTIR) for glass and glass ceramic were due to the SiO_4 group. The optical properties were investigated using ultraviolet-visible (UV-Vis) absorption spectra. The optical band gap energies for glasses were also calculated, revealing $E_{opt}=1.9$ for $X=0$ and increased to 3.45 eV for $X=0.1$, i.e., located in the semiconductor range. The photoluminescence (PL) properties and CIE chromaticity diagrams of the as-prepared mica glasses and transparent glass ceramic revealed variation in color from pale purple to blue and light blue. These results indicate that the prepared mica materials can be used in different applications.

Keywords Mica · copper oxide · photoluminescence · transparent glass ceramics · nanocrystals · semiconductor

Introduction

Fluoromica glass ceramics can be seen as promising materials for different engineering and medicine applications. They are characterized by easy machinability, biocompatibility, and high dielectric constant.^{1,2} They are also heat-resistant above 800°C and have low porosity.³ These properties mainly depend on the structure and morphology of the mica crystals.⁴ Mica, which is a layered silicate mineral, can be seen as a 2D sheet.⁵ It usually takes the shape of a hexagonal sheet array. Any form has a complete cleavage that is very thinly peeled off.⁶ Two-dimensional nanosheets have a propensity to display isotropic properties. This is because their vertical and planar physical and chemical properties differ from those of nanostructures in other dimensions (i.e., 0D, 1D, and 3D).^{7,8} The 2D nanosheet structure is broadly used in applications such as insulation,⁹ electronics, catalysis,

sensing, and solar cell technology.^{10–13} On the other hand, fluoride glasses have important benefits. They are characterized by high transparency in the infrared (IR) region of the spectrum and low phonon energies. These properties qualify them to be used for amplification of light in telecommunications systems¹⁴; however, their chemical durability is low. Oxyfluoride glass ceramics combine the optical properties of fluoride glasses with the simplicity of forming and treatment of conventional oxide glasses.^{14,15} Luminescent oxyfluoride glass ceramics have recently attracted the interest of researchers, owing to their excellent luminous efficiency as well as energy-saving and eco-friendly properties.¹⁶ Luminescent oxyfluoride glass ceramics can convert most exciting energies into visible emissions, and therefore have important applications in lighting, display devices, and optical communication.^{17,18}

Low cost, excellent luminescence efficiency, adjustable emission colors, low toxicities, and great photo-stability are all advantages of transition metal ion-based nanophosphors.^{19,20} Among these, copper ion is a competent activator, producing green and blue emissions in light-emitting devices.^{21,22} The luminescence of Cu^+ ion corresponds to the $3d^9 4s^1 \rightarrow 3d^{10}$ transition, the 4s outer electrons are sensitive

✉ M. A. Ouis
mennay@yahoo.com

¹ Glass Research Department, National Research Centre, Dokki, Giza, Egypt

to the neighboring structure. This results in strong deviation of the luminescence properties of Cu^+ with different glass structures.²³

Copper ion probably exists as metallic Cu, cuprous Cu^+ , or cupric Cu^{2+} in the silicate glass matrices.²⁴ Electrical, optical, mechanical, and chemical properties as well as the glass-forming ability of the glass system can be affected by the valence state of copper.^{25,26} During the crystallization process, the formation of copper nanoclusters were expected. The absorption bands at characteristic surface plasma resonance in the visible region and optical nonlinearity are displayed by these nanocrystals.^{27–29} Consequently, doping glass ceramics with copper ions in different oxidation states is extremely beneficial for use in electrical memory switching devices.²⁴

Herein, we prepare oxyfluoride glass ceramics based on mica structure doped with different concentrations of copper oxide. The effect of gradual replacement of Na with Cu ions on the structural $\text{Na}_{(1-x)}\text{Cu}_x\text{Mg}_3\text{AlSi}_3\text{O}_{10}\text{F}_2$ and luminescent properties was investigated. Also, the effect of heat treatment to obtain transparent glass ceramic was adjusted. Powder x-ray diffraction (XRD), Fourier transform infrared (FTIR) analysis, absorption optical studies, and photoluminescence (PL) spectroscopy were used in this investigation. According to the findings, the produced transition metal ion-doped phosphors could be beneficial in both light-emitting and display systems.

Experimental

Preparation of Glasses

Glasses were prepared with the chemical composition based on the stoichiometric formula $\text{Na}_{(1-x)}\text{Cu}_x\text{Mg}_3\text{AlSi}_3\text{O}_{10}\text{F}_2$, listed in Table I. The starting raw materials include laboratory reagent-grade Na_2CO_3 , CuO, MgCO_3 , MgF_2 , Al_2O_3 and SiO_2 ; about 25 g of glass was prepared from each composition, which were denoted as X0, X0.05, X0.07, and X0.1 according to the amount of copper oxide added. The accurately weighed batches were placed in a platinum crucible and melted in an electric furnace at 1400–1500°C for 1 h. The crucible was rotated every 15 min to reach complete mixing and homogeneity. The melts were poured onto a cold stainless-steel plate to ascertain their glassy nature.

Table I The stoichiometric chemical composition of different Cu-doping glasses in moles

Sample symbol	Na_2O	MgF_2	MgO	Al_2O_3	SiO_2	CuO
X0	0.5	1	2	0.5	3	–
X0.05	0.45	1	2	0.5	3	0.05
X0.07	0.43	1	2	0.5	3	0.07
X1	0.40	1	2	0.5	3	0.1

Crystallization of Glasses

Crystallization was performed according to the data obtained from differential thermal analysis (DTA) measurements that were carried out using a model Q600 SDT device. The applied heating rate was 10°C/min with alumina as a blank reference material. Both glass transition and crystallization temperatures were used to design a suitable heat treatment program for the prepared glasses.

X-ray Diffraction Analysis (XRD)

The prepared glass–ceramics were subjected to powder x-ray diffraction using Ni-filled $\text{Cu-K}\alpha$ radiation using Bruker D8 to identify crystalline phases formed by thermal heat treatment.

Optical UV–Visible Near-Infrared (NIR) Absorption Studies

UV-visible absorption spectra were detected for all glass samples. Highly polished glasses of equal thickness (2 mm \pm 0.1 mm) were scanned in the range of 200–1000 nm using a recording spectrophotometer (JASCO V-630, Japan).

Fourier Transform Infrared (FTIR) Absorption Spectra

The FTIR absorption for the prepared glasses were measured at room temperature in the range 4000–400 cm^{-1} by an infrared spectrophotometer (JASCO FT/IR-300E, Japan), using the KBr disc technique. Two milligrams of powdered glass were mixed with 200 mg of KBr and the mixture was subjected to a load of 5 tons/ cm^2 in order to produce clear homogeneous discs. The IR absorption spectra were measured immediately after preparing the desired discs. The same measurements were repeated for glass ceramic samples.

Luminescence Properties

PL was measured at room temperature using spectrofluorometer (Jasco FP-6500, Japan). The light source was a xenon arc lamp (150 W), and the excitation and emission slit band widths were both 5 nm.

CIE 1931 Chromaticity Diagram

Any color with its hue, saturation, and luminance can be specified by the tristimulus values X , Y , and Z . Chromaticity coordinates are calculated from the spectral power distribution of the light source and the CIE color-matching functions in the range 380–370 nm at intervals of 5 nm. The tristimulus values for a non-monochromatic light source with spectral relative power $P(\lambda)$ are given by^{30–32}:

$$X = \int P(\lambda)x(\lambda)d\lambda \quad (1)$$

$$Y = \int P(\lambda)y(\lambda)d\lambda \quad (2)$$

$$Z = \int P(\lambda)z(\lambda)d\lambda \quad (3)$$

where X , Y , and Z are the tristimulus values, which give the power for each of the three primary colors to match with the color of $P(\lambda)$, and from the tristimulus values the color chromaticity coordinates x and y can be determined using the following expression^{30,31}:

$$x = X/X + Y + Z \quad (4)$$

$$y = Y/X + Y + Z \quad (5)$$

$$z = Z/X + Y + Z \quad (6)$$

All the multichromatic wavelengths are expected to lie within the area of the chromaticity diagram. The luminescent intensity of the emission spectral measurements can be characterized using the CIE 1931 chromaticity diagram. These chromaticity coordinates are not linearly independent of each other, since they follow that $x + y + z = 1$ for all colors; it is therefore only necessary to quote two of the chromaticity coordinates, and these can of course be plotted on a normal two-dimensional graph.

Results and Discussion

Differential Thermal Analysis (DTA)

Differential thermal analyses (DTA) of un-doped and Cu-doped glasses are shown in Fig. 1. DTA thermograms revealed a broad endothermic effect corresponding to glass transition (T_g) at 598–600°C followed by a significant exothermic peak at 680–700°C corresponding to crystallization temperature (T_c). A slight decrease in both T_g and T_c were

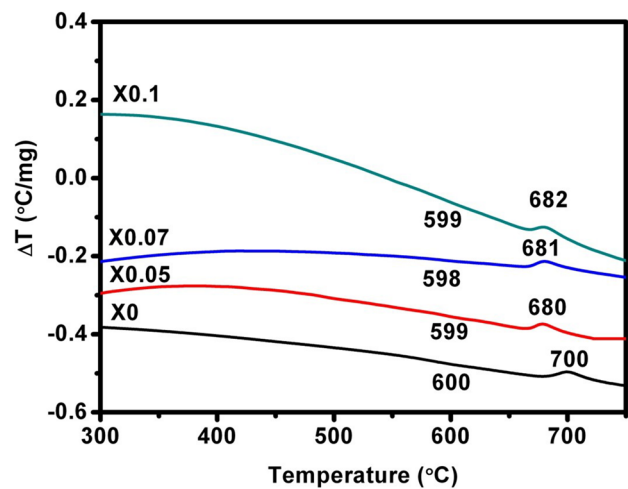


Fig. 1 DTA thermograms for as-quenched glasses with different Cu additions.

observed after adding CuO. This decrease can be attributed to a decrease in viscosity by replacing Na^+ , which has an ionic radius of $\sim 1.8 \text{ \AA}$, with Cu^{2+} , which has a smaller ionic radius of $\sim 1.35 \text{ \AA}$, through an increase in temperature.³³ This replacement will facilitate the mobility of ions leading to a slight decrease in both T_g and T_c as well as enhancing the degree of crystallization,^{34,35} as will be shown later by XRD.

X-ray Powder Diffraction

The prepared glasses were exposed to two different heat treatment schedules. The first consists of one step at 750°C/4 h; this temperature covers the exothermic peak range so it will provide a complete picture about the developed crystallized phases. The second program consists of two steps, one at 550°C/4 h and the second at 650°C/0.5 h, for studying the effect of heat treatment at nucleation temperature for a long period, which will induce a large number of nuclei, followed by heat treatment at the onset temperature of the crystallization peak to obtain the smallest-sized crystals of the desired phase. This schedule aims to obtain transparent glass ceramic. The XRD analysis of the samples after the two heat treatment programs is displayed in Figs. 2 and 3.

XRD after heat treatment at 750°C/4 h (Fig. 2) revealed, in general, crystallization of mica ($\text{NaAl}_3\text{Si}_3\text{O}_{11}$), MgF_2 , and pyrope ($\text{Mg}_3\text{Al}_2\text{Si}_3\text{O}_{12}$), where the XRD Bragg peaks are matched with ASTM cards no. 46-0740, 1-1196, and 89-1490 in that order. Gradual replacement of Na^+ with Cu ions lead to enhancement the crystallization of both mica and pyrope while MgF_2 disappeared. This is mirrored by increasing the intensity of XRD peaks correspond to mica and pyrope; while XRD peaks corresponding to MgF_2 vanished. This can be explained as follows: with increasing CuO

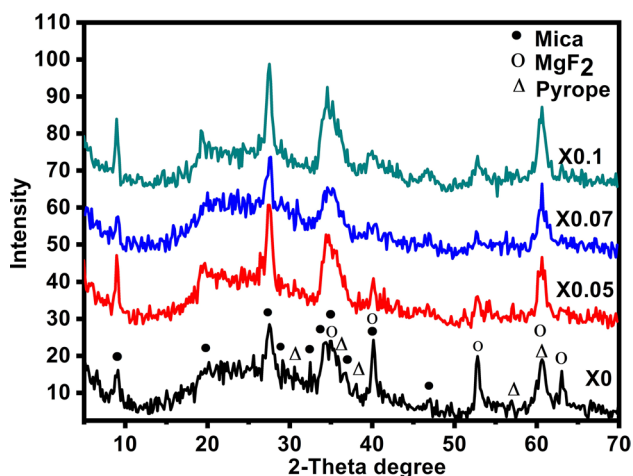


Fig. 2 XRD analysis of glass ceramic samples after heat treatment at 750°C/4 h.

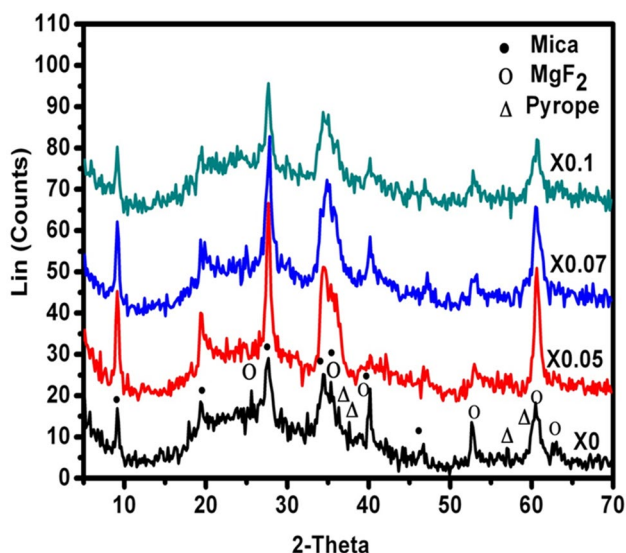


Fig. 3 XRD analysis of glass ceramic samples after heat treatment at 550°C/4 h+650°C/0.5 h.

the viscosity of the glass decreased and the mobility of ions increased, so Mg^{2+} of MgF_2 reacted more easily with the remaining Al^{3+} and Si^{4+} to obtain pyrope phase.

Unlike the expected results, a small shift in d-spacing to higher values is observed by increasing the addition of Cu ions. If Cu ions, which have a small ionic radius of $\sim 1.35 \text{ \AA}$, replace Na ions, with a higher ionic radius of $\sim 1.8 \text{ \AA}$, in its position in the mica structure, the expected result is a shift in d-spacing toward smaller values. However, the contrary is observed, which means that Cu ions are not included in the mica structure, and the increase in d-spacing is due to greater development of the crystal structure as a result of the enhanced crystallization process with an increase in Cu ions.³⁶ On the other hand, no copper-bearing phases are

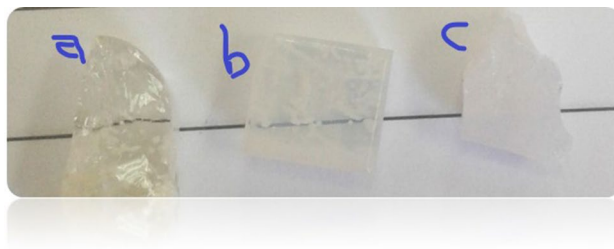


Fig. 4 Visual image of (a) X0 glass as quenched, (b) after heat treatment at 550°C/4 h then at 650°C/0.5 h, and (c) after heat treatment at 750°C/4 h.

detected by XRD, which may be due to the reduction of copper ions during heat treatment by F^- to copper metal, which was ejected out to the surface of the sample.

The XRD spectra of samples heat-treated at 550°C/4 h+650°C/0.5 h are illustrated in Fig. 3, which reveals the same behavior of the sample heat-treated at 750°C for 4 h but with higher Bragg peak intensity, indicating an increase in the degree of crystallization. This can be attributed to the fact that the crystallization process is carried out in bulk mode (homogeneous nucleation), not surface mode, so heat treatment at 550°C/4 h enhanced the pre-crystallization step, i.e., formation of a huge number of nuclei, and after increasing the temperature to 650°C for only 0.5 h, the development of crystallized phases with small size is obtained. There are no observed shifts in d-spacing, as in samples heat-treated at 750°C/4 h, due to the limited growth of the crystals through this heating schedule. Consequently, this program is successful in producing transparent glass ceramic as shown in Fig. 4, where the visual appearance of the as-prepared glass (X0) and that after heat treatment at both 550°C/4 h+650°C/0.5 h and 750°C/4 h is shown. The as-prepared glass looks yellowish transparent and after 550°C/4 h+650°C/0.5 h looks whitish transparent, while after 750°C/4 h it appears opaque.

In both heat treatment programs cited above, increasing XRD intensity with a gradual increase in CuO is observed. This may be due to the transition metal ions that are commonly used as crystal stimulators for controlled crystallization processes, giving rise to huge numbers of nucleation centers in the original glass.²⁴

Using the Debye-Scherrer formula, the average crystallite sizes are determined from the most intense XRD peaks, as follows: $D = k\lambda/B \cos\theta$ where D is the particle size, k is a constant, λ for Cu is 1.54 \AA , B is the full width at half maximum, and $2\theta = 4^\circ$. The crystallite size is in the nanoscale, recorded as $\sim 15 \text{ nm}$, 14 nm , 13 nm , and 11 nm for X0, X0.5, X0.07, and X0.1, respectively. The decrease in crystal size with increased CuO addition is due to the role played by

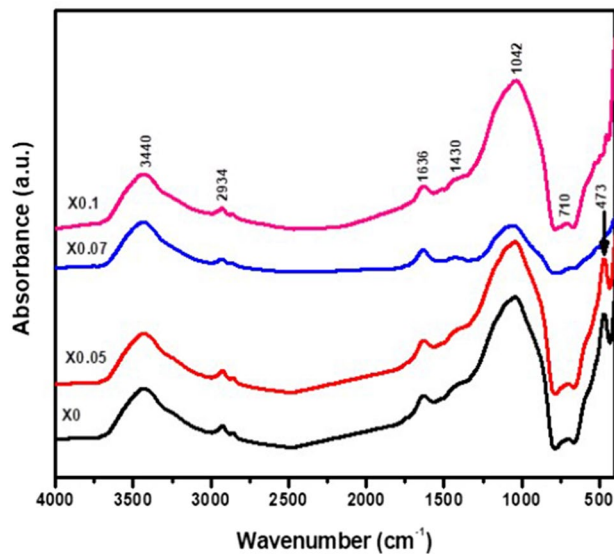


Fig. 5 FTIR absorption spectra of the as-prepared glasses.

CuO as nucleating agent; as CuO increases, the number of nuclei increases, preventing further crystal growth.

Fourier Transform Infrared (FTIR) Absorption Data

Infrared spectroscopy is a very valuable analytical technique. It gives convenient evidence about structural building units in various oxide glasses.³⁷ Figure 5 shows the FTIR absorption spectra of the prepared glasses. The main structural unit in the prepared glass is SiO_4 . Therefore, most of the bands that appear are due to silicate group networks. The vibrational bands of silicate chains are active in the spectral region between 400 cm^{-1} and 1600 cm^{-1} .³⁸ Peaks owing to water or hydroxyl (OH) and silanol (SiOH) group vibrations can be seen in the NIR spectral region from 2000 cm^{-1} to 4000 cm^{-1} .³⁸ Molecular water vibrations are responsible for the tiny peak at around 1636 cm^{-1} . Water and OH vibrations are responsible for the two tiny peaks at 2934 cm^{-1} .³⁹ Molecular water vibrations are responsible for the large peak at the IR band at 3440 cm^{-1} . The small curvature at 1400 cm^{-1} is due to the carbonate group. The peak at 1042 cm^{-1} is due to Si-O-Si asymmetric stretching. The peak at 710 cm^{-1} is due to symmetric stretching of the Si-O-Si group. The peak at 473 cm^{-1} is due to bending vibrations of Si-O-Si and O-Si-O linkages.⁴⁰ It can also be attributed to MgO or Na_2O .³⁹

The FTIR absorption spectra after heat treatment at $750^\circ\text{C}/4\text{ h}$ are shown in Fig. 6. The small shift in band positions is due to changes in the bond strength, which is caused by strain in the chemical bonds. Consequently, the shift in band positions can be attributed to the formation of different phases causing distortions of the SiO_4 tetrahedra. The

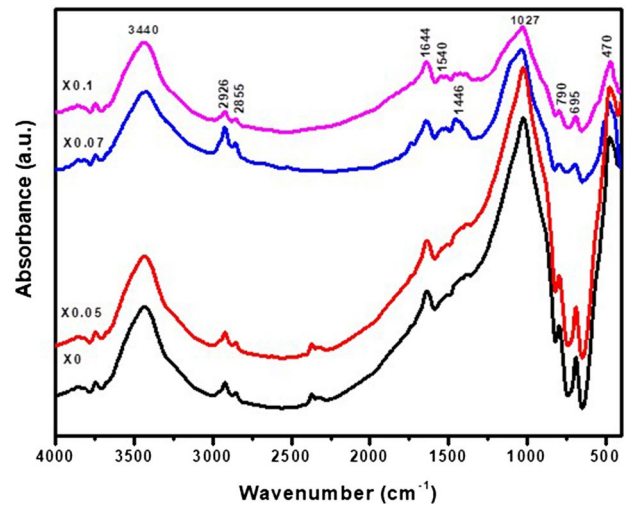


Fig. 6 FTIR absorption spectra of prepared glass ceramics heat-treated $750^\circ\text{C}/4\text{ h}$.

band at 1430 cm^{-1} splits into two small bands at 1446 cm^{-1} and 1540 cm^{-1} . The band at 1042 cm^{-1} shifts to a lower wavelength at 1027 cm^{-1} . The peak at 710 is shifted to 790 cm^{-1} and a peak appears at 695 cm^{-1} . The peak at 473 cm^{-1} shifts to 470 cm^{-1} .

It appears from the results that the progressive additions of copper oxide do not affect the FTIR absorption bands for either glass or glass ceramic. This may be due to the very small amount of copper added to the prepared glasses. This confirms the presence of CuO in the interstitial position and not in the main structural units in the mica glass ceramic lattice.⁴⁰

Optical Absorption Measurements

UV-radiation excites valence electrons in the irradiated material and complicated photoreaction processes led subsequently to the formation of irradiation-induced defects. Defects are generated in ppm concentrations and occur in pairs of positive hole centers (HC) with negative electron centers (EC). While the extrinsic defects are connected to dopants or impurities, the intrinsic defects arise from the glass matrix itself. The formation of defects may result in transmission changes but also in changes in the refractive properties of the material.⁴¹ Between many transition ions, the dissolution of minor amounts of copper ions in glass matrices makes the glasses colored and strongly affects the structural and optical properties.⁴²

Copper is usually found in glasses as Cu^+ ($3d^{10}4s^0$) or as Cu^{2+} ion ($3d^94s^0$). The sample is light blue in color, and the optical spectrum shows a broad absorption with a maximum around 800 nm (Fig. 7). The broadness of the d-d transition band is caused by Jahn-Teller distortion of Cu^{2+} (d^94s^0).⁴³

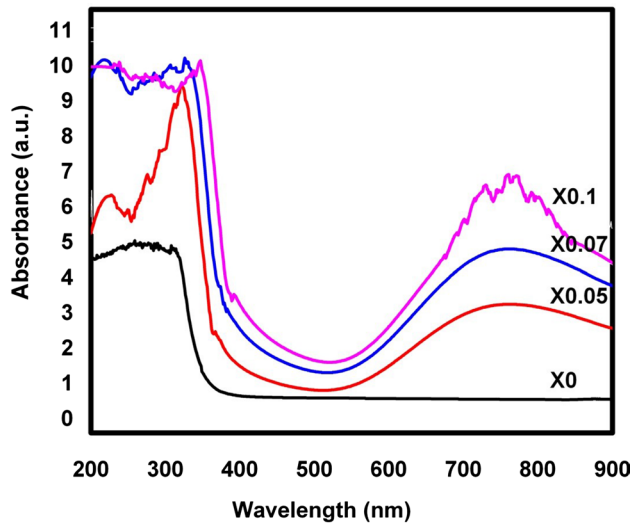


Fig. 7 UV-visible absorption spectra of the as-prepared glasses.

At 250 nm, the base glass produces a prominent band. UV absorption peaks between 285 nm and 320 nm, with a large curve of about 420 nm, followed by a very broad band with nearly the same intensity and position as the peak at 750 nm, which is linked to octahedrally coordinated Cu^{2+} ions.³⁸ As the mol% of CuO is increased from 0.05 to 0.1 in the glass samples, the main UV absorption band at 750 nm becomes higher and sharper. The existence of electron-trapped centers, such as SiO_4 and oxygen-related hole centers, causes an increase in the absorption at wavelengths < 300 nm.⁴⁴ The UV absorption edges of copper-doped glass samples red-shifted as the CuO doping concentration increased.²³

Optical Band Gap Energy

The absorption coefficient α at the absorption curve's edge is used to calculate the optical band gap energy of the prepared glasses. The absorption coefficient is calculated using the formula below⁴⁵:

$$\alpha = \frac{2.303A}{t}$$

For each sample, A is the absorbance and t is the thickness in cm. The following equation describes the relationship between α and the photon energy of incident radiation, $h\nu$ ⁴⁶:

$$\alpha h\nu = B(h\nu - E_{opt})^r$$

where B is a constant, E_{opt} is the energy of the optical band gap, and r is an index, taking the values (2, 3, 1/2, or 3/2) corresponding to indirect allowed, indirect forbidden, direct allowed, and direct forbidden transitions, respectively.⁴⁷ The

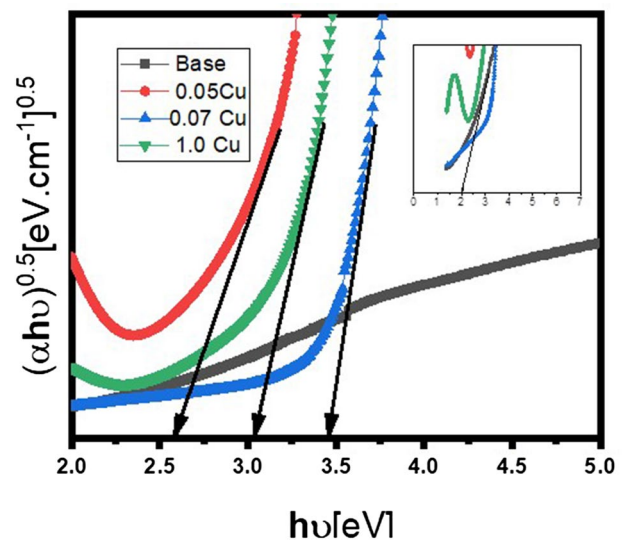


Fig. 8 Optical band gap energy for glasses with different Cu additions.

optical band gap values are calculated by extrapolating the linear region of the $(\alpha h\nu)^{1/2}$ vs. $h\nu$ plots (Fig. 8). The value of E_{opt} obtained is 1.9 eV for the Cu-free sample, X0. The gradual addition of Cu ions leads to a gradual increase in E_{opt} to 2.58 eV, 3.02 eV, and 3.45 eV for X0.05, X0.07, and X0.1, respectively. It is observed that the optical band gap (E_{opt}) is increased with an increase in CuO content. The optical band gap (E_{opt}) is proportional to the compactness of the network structure. The glass network becomes more compact as the average number of bridging atoms increases, resulting in an increase in the optical band gap.⁴⁷ Cu ions form stronger connections with oxygen in this glass composition than Na ions do. Subsequently, a more dense texture appeared in the X0.1 sample than in X0.07 and X0.05, with lower CuO content. As a result, the substitution of CuO for Na_2O in this glass composition increases the optical band gap (E_{opt}). From a different perspective, the drop in optical band gap energy corresponds to a decrease in phonon-assistant indirect transitions.⁴⁸ The optical band gap (E_{opt}) values for all glasses are in the semiconductor region in general.

PL Behavior of the Glasses

PL emission spectra of glasses and glass ceramics at room temperature after heat treatment at $550^\circ\text{C}/4\text{ h}+650^\circ\text{C}/0.5\text{ h}$, excited at $\lambda_{ex}=315\text{ nm}$ are shown in Figs. 9 and 10.

The PL emission spectra of the glasses (Fig. 9) revealed that copper-free glass exhibited six bands, as follows:

- (a) Three intense bands at 326 nm, 404 nm, and 465 nm (in the range of UV, violet, and blue, respectively).

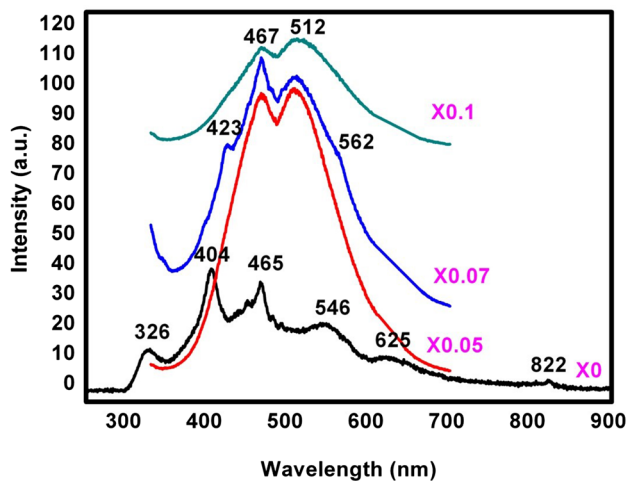


Fig. 9 The photoluminescence spectra of as-quenched glasses.

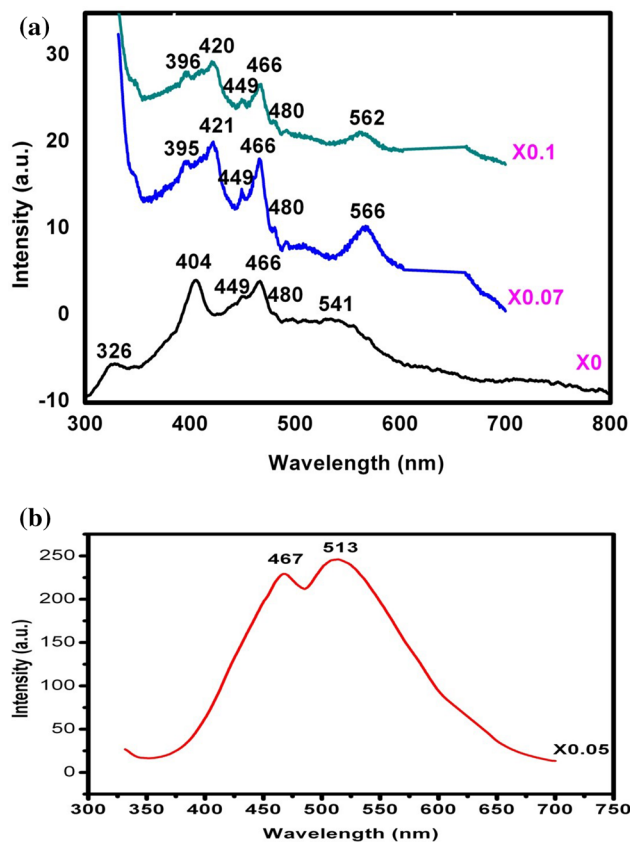


Fig. 10 The photoluminescence spectra of glass ceramic after heat treatment at 550°C/4 h+650°C/0.5 h (a) for samples X0, X0.07, X1.0, and (b) for sample X0.05.

- (b) Two broad bands at 546 nm and 625 nm (in the range of green and orange).
 (c) Very small band at 822 nm (NIR range).

Adding CuO led to a change in this behavior, where two very intense bands at 467 nm (blue) and 512 nm (green) appeared in the X0.05 sample. This intensity decreased with the increased addition of CuO. Small kinks appeared in only the X0.07 sample at both 423 nm (indigo) and 562 nm (green).

The PL emission spectra of the transparent glass ceramic after heat treatment at 550°C/4 h+650°C/0.5 h are shown in Fig. 10a, b. Both X0.07 and X0.1 glass ceramics revealed the same behavior, where three intense bands at 466 (blue), 421 (violet), and 566 nm (green) appeared and three kinks at 395 (violet), 449 (blue), and 480 nm (blue) also appeared; the intensity decreased with increased CuO addition, as shown in Fig. 10a. The copper-free glass ceramic depicted almost the same PL spectra as its parent glass but with lower intensity. The X0.05 glass ceramic revealed highly intense bands at both 467 (blue) and 512 nm (green) the same as its parent glass but with higher intensity, as shown in Fig. 10b.

It is observed that copper-free mica glass and glass ceramic revealed a wide PL emission spectrum, from UV range (326 nm) to the NIR range (822 nm), and visible emission at violet (404 nm), blue (465 nm), green (546 nm), and orange (625 nm). We can consider that pure mica glass exhibited PL properties over a wide range; these results are matched with other previous studies.⁴⁹

It is known that Cu ions have strong luminescence intensity in the visible light region among different transition metals.^{50–52} The luminescence of Cu⁺ ions corresponds to the 3d⁹4s¹→3 d¹⁰ transition, and the 4s outer electrons are sensitive to the surrounding structural environment. This can result in a strong variation in the luminescence properties of Cu⁺ with the glass matrix.²³ Gradual addition of CuO results in a significant change in PL emission, where the predominant luminescence is due to the CuO addition. The change in luminescence spectra indicates the transformation of luminescence centers or changes in their concentrations.⁵³

Copper can exist as ions, atoms, charged or neutral nano-sized molecular clusters (MCs), and nanoparticles.⁵³ PL emissions of copper-doped mica glasses reveal two main emission peaks located at 467 nm and 512 nm; compared with the literature,²³ these values are red-shifted (~450 nm and 505 nm, respectively²³). The red shift occurs because the increased concentration of CuO reduces the distance between the Cu⁺ ions and increases the possibility of overlapping of the S excited state. As a result, the S excited state is very close to the ground state, causing the red-shift effect.²³ Cu⁺ ions isolated in the visible area can emit luminescence with a wavelength of approximately 467 nm. The peak at 512 nm is due to the high concentration of CuO, which lead to a decrease in the distance between two Cu⁺ forming Cu⁺-Cu⁺ ion pairs.²³ The luminescence of the Cu⁺ ion can be explained in two ways. The luminescence of Cu⁺ ion monomer and dimer⁵⁴ is one of them. A side from Cu⁺

ion luminescence in an eight-coordinated cube and a six-coordinated octahedral.⁵⁵ Another explanation is due to the relationship between them. The Cu^+ ion monomer is thought to occupy the centers of the eight-coordinated cube, while the Cu^+ ion dimer is thought to occupy the six-coordinated octahedral.²³ The emission intensity of Cu^+ ions increased first and then declined as the Cu^+ ion quantity increased, reaching a maximum at $X=0.05$. Concentration quenching occurs at this optimal concentration. Increasing the CuO addition leads to the appearance of two kinks at 423 nm and 562 nm in $X0.07$ and more broad bands in $X0.1$. The reason for this phenomenon may be due to when the concentration of CuO is high, the isolated Cu^+ ions transfer energy to the Cu^+-Cu^+ ion pairs.²³

After heat treatment, noticeable changes in PL properties were observed. All samples, except $X0.05$, revealed PL emission spectra similar to cooper-free mica glass ceramic; i.e., the effect of copper was not noticeable. These results can be interpreted as follows: During heat treatment, the reduction

process of Cu^+ due to the presence of F^- and electrons was increased. Consequently, all Cu^+ was transformed into neutral MCs, which were ejected from the bulk sample to the surface.^{56,57}

Figure 11a and b show the CIE chromaticity diagrams which give the change in color with CuO addition in the glass and glass ceramics, respectively. The variation in color from pale purple to blue and light blue indicates that these prepared mica materials can be used in different applications.

Conclusions

Mica-based glasses in a $\text{Na}_{(1-x)}\text{Cu}_x\text{Mg}_3\text{AlSi}_3\text{O}_{10}\text{F}_2$ system were synthesized by an ordinary melting technique. The effects of different amounts of copper oxide on the optical and PL properties of mica glasses and glass ceramics were investigated. X-ray diffraction illustrated crystallization of mica ($\text{NaAl}_3\text{Si}_3\text{O}_{11}$), MgF_2 and pyrope ($\text{Mg}_3\text{Al}_2\text{Si}_3\text{O}_{12}$). As the addition of CuO was increased from 0.05 to 0.1, the characteristic UV absorption bands become higher and sharper. Progressive additions of CuO did not affect the intensity or position of the peaks in the FTIR spectra for either the glass or glass ceramic. CIE chromaticity diagrams revealed variation in color from pale purple to blue and light blue, thus indicating that the prepared mica materials can be used in different applications.

Conflict of interest The authors have no conflicts of interest to declare that are relevant to the content of this article.

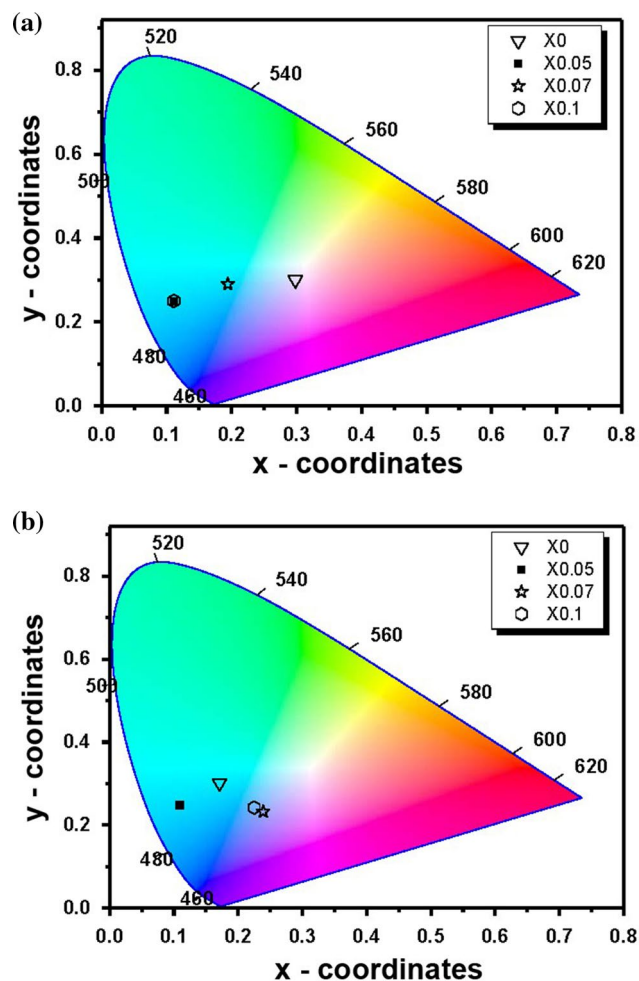


Fig. 11 CIE chromaticity diagram representing colors of the light emitted from the investigated (a) glasses and (b) glass ceramics after heat treatment at $550^\circ\text{C}/4$ h and then at $650^\circ\text{C}/0.5$ h.

References

1. B. Eftekhari Yekta and Z. Hamnabard, Investigation of the mechanical properties and machinability of fluorphlogopite-gehlenite glass-ceramics. *Int. J. Appl. Ceram. Technol.* 6, 72 (2009).
2. M. Romero and J.M. Rincon, Development of mica glass-ceramic glazes. *J. Am. Ceram. Soc.* 87, 819 (2004).
3. G. S. Upadhyaya, Holland W., Beall G.: Glass-ceramic technology, "The American Ceramic Society", Westerville, OH, USA, 2002, pp. 372. *Sci. Sinter.* 36 (3), 215–216 (2004).
4. S. Habelitz, G. Carl, C. Riissel, S. Thiel, U. Gerth, J.D. Schnapp, A. Jordanov and H. Knake, Mechanical properties of oriented mica glass ceramic. *J. Non-Cryst. Solids.* 220, 291 (1997).
5. A. Castellanos-Gomez, M. Poot, A. Amor-Amorós, G. Steele, H. Zant, N. Agrait and G. Rubio-Bollinger, Mechanical properties of freely suspended atomically thin dielectric layers of mica. *Nano Res.* 5, 550 (2012).
6. S. Park, Y. Min Byoun, H. Gil Na, M. Kim, S. Choi and Ch. Jin, Characterization of luminescence properties of exfoliated mica via sonication technique. *Chem. Phys.* 522, 238 (2019).

7. M. Leng, Y. Chen and J. Xue, Synthesis of TiO₂ nanosheets via an exfoliation route assisted by a surfactant. *Nanoscale* 6, 8531 (2014).
8. X. Huang, Z. Zeng and H. Zhang, Metal dichalcogenide nanosheets: preparation, properties and applications. *Chem. Soc. Rev.* 42, 1934 (2013).
9. S.A.M. Abdel-Hameed, N. Ismail, H.F. Youssef, H.E.H. Sadek and M.A. Marzouk, Preparation and characterization of mica glass-ceramics as hydrogen storage materials. *J. Hydrog. Energy* 42, 6829 (2017).
10. L. Sheng, T. Liao, L. Kou and Z. Sun, Single-crystalline ultrathin 2D TiO₂ nanosheets: a bridge towards superior photovoltaic devices. *Mater. Today Energy* 3, 32 (2017).
11. J. Gunjaker, I. Kim, J. Lee, N. Lee and S. Hwang, Self-assembly of layered double hydroxide 2D nanoplates with graphene nanosheets: an effective way to improve the photocatalytic activity of 2D nanostructured materials for visible light-induced O₂ generation. *Energy Environ. Sci.* 6, 1008 (2013).
12. J. Zhou, J. Qin, X. Zhang, C. Shi, E. Liu, J. Li, N. Zhao and C. He, 2D space-confined synthesis of few-layer MoS₂ anchored on carbon nanosheet for lithium-ion battery anode. *ACS Nano* 9, 3837 (2015).
13. I. Moon, J. Kim, H. Lee, K. Hur, W. Kim and H. Lee, 2D graphene oxide nanosheets as an adhesive over-coating layer for flexible transparent conductive electrodes. *Sci. Rep.* 3, 1112 (2013).
14. G.H. Beall and L.R. Pinckney, Nanophase glass-ceramics, Nanophase glass-ceramics. *J. Am. Ceram. Soc.* 82, 5 (1999).
15. F.H. Margha, S.A.M. Abdel-Hameed, N.A. Ghoniem, S. Satokawa and T. Kojima, Crystallization behavior of new transparent glass-ceramics based on barium borate glasses, *Journal of the. Ceram. Soc. Jpn.* 116, 624 (2008).
16. R. Koutavarapu, Ch. Reddy, M.C. Rao, R.S.N. Ravikumar and M. Cho, Structural, optical, and luminescence properties of Cu²⁺-doped Ca-Li hydroxyapatite nanopowders prepared by mechanochemical synthesis. *J. Shim Mater. Res. Express* 6, 105046 (2019).
17. B. Ramesh, G.R. Dillip, G.R. Reddy, B.D.P. Raju, S.W. Joo, N.J. Sushma and B. Rambabu, Luminescence properties of CaZn₂(PO₄)₂: Sm³⁺ phosphor for lighting application. *Optik* 156, 906 (2018).
18. Z. Xia, Z. Xu, M. Chen and Q. Liu, Recent developments in the new inorganic solid-state LED phosphors. *Dalton Trans.* 45, 11214 (2016).
19. F. Kang, M. Peng, Q. Zhang and J. Qiu, Broadly tuning Bi³⁺ emission via crystal field modulation in solid solution compounds (Y, Lu, Sc)VO₄: Bi for ultraviolet converted white LEDs. *Chem. Eur. J.* 20, 11522 (2014).
20. V. Khidhirbrahmendra, S.J. Basha, M. Avinash and R.V.S. Ravikumar, Investigations of VO²⁺ doped SrZn₂(PO₄)₂ nanophosphors by solution combustion synthesis. *J. Alloys Compd* 787, 276 (2019).
21. R. Stella, G. Rao, B. Babu, V. Pushpa Manjari, C.V. Reddy, J. Shim and R.V.S. Ravikumar, A facile synthesis and spectral characterization of Cu²⁺ doped CdO/ZnS nanocomposite. *J. Magn. Mater.* 384, 6–12 (2015).
22. V.P. Manjari, C.R. Krishna, C.V. Reddy and R.V.S. Ravikumar, Synthesis and spectral investigations of Cu (II) ion-doped NaCaAlPO₄F₃ phosphor. *Luminescence* 29, 1123 (2014).
23. Y. Dua, J. Yuana, Sh. Hana, S. Yana, Y. Wanga and D. Chena, Luminescence and scintillation properties of CuO-doped SiO₂-B₂O₃-La₂O₃ glass. *Opt. Mater.* 96, 109363 (2019).
24. T. Srikumar, I.V. Kityk, Ch. SrinivasaRao, Y. Gandhi, M. Piasecki, P. Bragiel, V. Ravi Kumar and N. Veeraiyah, Photostimulated optical effects and some related features of CuO mixed Li₂O-Nb₂O₅-ZrO₂-SiO₂ glass ceramics. *Ceram. Int.* 37, 2763 (2011).
25. T. Miura, T. Watanabe, Y. Benino, T. Komatsu and R. Sato, Unusual elastic and mechanical behaviors of copper phosphate glasses with different copper valence states. *J. Am. Ceram. Soc.* 84, 2401 (2001).
26. E. Cattaruzza, G. Battaglin, F. Gonella, R. Polloni, B.F. Scremin, G. Mattei, P. Mazzoldi and C. Sada, Au-Cu nanoparticles in silica glass as composite material for photonic applications. *Appl. Surf. Sci.* 254, 1017 (2007).
27. B. Karthikeyan, M. Anija and C.S. Suchand Sandeep, Optical and nonlinear optical properties of copper nanocomposite glasses annealed near the glass softening temperature. *Opt. Commun.* 281, 2933 (2008).
28. R. Kibar, A. Cetin and N. Can, Effect of thermal treatment on linear optical properties of Cu nanoclusters. *Phys. B* 404, 105 (2009).
29. J. Sheng, S. Chen, J. Zhang and J.Yu. Li Juan, UV-light irradiation induced copper nanoclusters in a silicate glass. *Int. J. Hydrog. Energy* 34, 1119 (2009).
30. D. Malacara, *Color Vision and Colorimetry: Theory and Applications*, 2nd ed., (Bellingham, Washington, USA: SPIE Press, 2011).
31. R.J. Mortimer and T.S. Varley, Quantification of colour stimuli through the calculation of CIE chromaticity coordinates and luminance data for application to *in situ* colorimetry studies of electrochromic materials. *Displays* 32, 35 (2011).
32. M.A. Marzouk and S.A.M. Abdel-Hameed, Crystallization and photoluminescent properties of Eu, Gd, Sm, Nd co-doped SrAl₂B₂O₇ nanocrystals phosphors prepared by glass-ceramic technique. *Luminescence* 205, 248 (2019).
33. G. Ravi Kumara, M. Gopi Krishna and M.C. Rao, Cr³⁺ doped NaF-ZrO₂-B₂O₃-SiO₂ glass ceramic materials for optoelectronic device application. *Optik* 173, 78 (2018).
34. S.A.M. Abdel-Hameed, M.A. Marzouk and A.E. Abdel-Ghany, Magnetic properties of nanoparticles glass-ceramic rich with copper ions. *J. Non-Cryst. Solids* 357, 3888 (2011).
35. S.A.M. Abdel-Hameed and A.M. ElKady, Effect of different additions on the crystallization behavior and magnetic properties of magnetic glass-ceramic in the system Fe₂O₃-ZnO-CaO-SiO₂. *J. Adv. Res.* 3, 167 (2012).
36. S.A.M. Abdel-Hameed, M.A. Marzouk and M.M. Farag, Effect of P₂O₅ and MnO₂ on crystallization of magnetic glass ceramics. *J. Adv. Res.* 5, 5543 (2014).
37. S.A. Ahmed, F.A. Mostafa and M.A. Ouis, Enhancement stability and catalytic activity of immobilized α-amylase using bioactive phospho-silicate glass as a novel inorganic support. *Int. J. Biol. Macromol.* 112, 371 (2018).
38. F.H. ElBatal, M.A. Ouis, A.M. Abdelghany and N.A. Ghoneim, Structural and optical correlation of gamma-irradiated 3d transition metals-doped lithium disilicate glasses. *SILICON* 7, 409 (2015).
39. S. ElShabrawy, C. Bocker and C. Rüssel, Crystallization of MgFe₂O₄ from a glass in the system K₂O/B₂O₃/MgO/P₂O₅/Fe₂O₃. *Solid State Sci.* 60, 85 (2016).
40. A.M. Abdelghany, F.H. ElBatal, H.A. ElBatal and F.M. EzzEl-Din, Optical and FTIR structural studies of CoO-doped sodium borate, sodium silicate and sodium phosphate glasses and effects of gamma irradiation-a comparative study. *J. Mol. Struct.* 1074, 503 (2014).
41. D. Möncke and D. Ehrhart, Charge transfer transitions in glasses - Attempt of a systematic review. *Opt. Mater.* X 12, 100092 (2021).
42. E. Metwalli, Copper redox behavior, structure and properties of copper lead borate glasses. *J. Non-Cryst. Solids* 317, 221 (2003).
43. D. Möncke and D. Ehrhart, *Photoionization of Polyvalent Ions* (Hauppauge: Nova Science Publishers Inc, 2007).
44. P. Ebeling, D. Ehrhart and M. Friedrich, X ray induced effects in phosphate glasses. *Opt. Mater.* 20, 101 (2003).

45. G.H. Zhang, K.C. Chou, U. Pal, 3rd Int. Conference on Molten Slags and Fluxes 85, 1988. " *ISIJ international* 53.5 (2013): 761–767 (2013)
46. D.P. Almond and C.R. Bowen, Anomalous power law dispersions in ac conductivity and permittivity shown to be characteristics of microstructural electrical networks. *Phys. Rev. Lett.* 92, 5 (2004).
47. Y.R. Luo, *Comprehensive Handbook of Chemical Bond Energies* (Boca, Raton: CRC Press, 2007).
48. S.P. Singh, B. Karmakar, Bismuth oxide and bismuth oxide doped glasses for optical and photonic applications. ISBN 978-1-61470-640-3 (2012).
49. S. Parka, Y. Byounb, H. Nac, M. Kimd, S. Choid and C. Jinc, Characterization of luminescence properties of exfoliated mica via sonication technique. *Chem. Phys.* 522, 238 (2019).
50. D. Ghosh, K. Biswas, S. Balaji and K. Annapurna, Tunable white light generation from Ce³⁺-Tb³⁺-Mn²⁺ doped metaphosphate glass for LED and solar cell applications. *J. Lumin.* 183, 143 (2017).
51. N. Abdedou, T. Djouama, M. Chalal, M. Poulain, B. Capoen and R. Mahiou, Synthesis and characterization of Er³⁺/Cu⁺-codoped fluorophosphate glasses. *J. Alloy. Comp.* 790, 248 (2019).
52. D.K. Xu, Y.F. Shi, X.S. Peng, R.F. Wei, F.F. Hu and H. Guo, Tunable broad photoluminescence in Cu⁺/Mn²⁺ co-doped oxyfluoride glasses sintered in air atmosphere. *J. Lumin.* 202, 186 (2018).
53. A.A. Murashova, A.I. Sidorova, M.V. Stolyarchuka and M.E. Boikob, Effect of X-ray irradiation and thermal treatment on luminescent properties of barium-phosphate glasses doped with silver and copper. *J. Non-Cryst. Solids* 477, 1 (2017).
54. Q. Zhang, G.R. Chen, G.P. Dong, G. Zhang, X.F. Liu, J.R. Qiu, Q.L. Zhou, Q.X. Chen and D.P. Chen, The reduction of Cu²⁺ to Cu⁺ and optical properties of Cu⁺ ions in Cu-doped and Cu/Al-co doped high silica glasses sintered in an air atmosphere. *Chem. Phys. Lett.* 482, 228 (2009).
55. R. Debnath and S.K. Das, Site-dependent luminescence of Cu⁺ ions in silica glass. *Chem. Phys. Lett.* 155, 52 (1989).
56. I.A. Demichev, A.I. Ignatiev, N.V. Nikonorov, E.M. Sgibnev, A.I. Sidorov and T.A. Khrushcheva, Specific features of the luminescence of silicate glasses with silver introduced by ion exchange. *Opt. Spectrosc.* 116, 587 (2014).
57. I.A. Demichev, A.I. Sidorov and N.V. Nikonorov, The influence of the conditions of ion exchange in CuSO₄:Na₂SO₄ melt on the optical properties of surface layers of silicate glass. *Opt. Spectrosc.* 119, 234 (2015).

Publisher's Note Springer Nature remains neutral with regard to jurisdictional claims in published maps and institutional affiliations.